Nitrogen isotopic fractionations in the low temperature (80K) vacuum ultraviolet photodissociation of N_2

Subrata Chakraborty[1*], Teresa L. Jackson[1], Bruce Rude[2], Musahid Ahmed[2] and M. H. Thiemens[1]

[1]University of California, San Diego, Department of Chemistry and Biochemistry, 9500 Gilman Drive, La Jolla, CA 92093-0356 (subrata@ucsd.edu)

[2]Lawrence Berkeley National Laboratory, 1 Cyclotron Road, Berkeley, CA 94720.

Abstract: *N_2 is a diatomic molecule with complex electronic structure. Interstate crossings are prominent in the high energy domain, introducing significant perturbations to the system. Nitrogen mainly photodissociates in the vacuum ultraviolet (VUV) region of the electromagnetic spectrum through both direct and indirect predissociation. Due to the complexity introduced by these perturbations, the nitrogen isotopic fractionation in N_2 photodissociation is extremely hard to calculate and an experimental approach is required. Here we present new data of N-isotopic fractionation in N_2 photodissociation at low temperature (80K), which shows a distinctly different ^{15}N enrichment profile compared to that at relatively higher temperatures (200 and 300 K). The new data is discussed in light of the knowledge of N_2 photochemistry and calculated photoabsorption cross-sections in the VUV. This data, important to understanding the N-isotopic compositions measured in meteorites and other planetary bodies, is discussed in light of the knowledge of N_2 photochemistry and calculated photoabsorption cross-sections in the VUV.*

I. INTRODUCTION

Nitrogen is the fifth most abundant element in the universe and an essential component as a prebiotic molecular building block. In interstellar clouds, nitrogen exists in atomic and molecular

forms (N and N_2) in gas-phase reservoirs. Atomic nitrogen is very reactive and takes part in chemical reactions leading to ammonia, nitriles, and other nitrogen compounds. No such reactions occur when nitrogen is in N_2 form. Nitrogen isotopic analyses of meteorites, terrestrial planets, atmospheres of giant planets and their moons, solar wind, comets, and interplanetary dust particles advance understanding of volatile chemistry and prebiotic processes in the early solar system [1].

Direct astronomical observations of N_2 is difficult because of the absence of strong pure rotational or vibrational lines. It is well studied through the electronic transitions at ultraviolet wavelengths [2, 3]. The isotopic inventory of nitrogen in astronomical environments is also reasonably well known [1, 4]. The solar system was formed with an initial $^{15}N/^{14}N$ ratio acquired from parent molecular clouds from the interstellar medium (ISM). The near-identical compositions measured in the solar wind and the Jovian atmosphere ($\delta^{15}N \sim -400$ ‰) may indicate the formation of the gas giant with the initial solar system materials of the same N-isotopic composition [5, 6]. Bulk meteorite analysis exhibits a variation in the range of few hundred permil in $\delta^{15}N$ (wrt to air-N_2) [7-9] with occasional exceptionally high values (as well as a range of variation) in some carbonaceous chondrites, stony-iron and iron meteorites. Conversely, extremely high ^{15}N enrichments are observed in meteoritic 'hotspots' (of ~5000‰ in some cases), interplanetary dust particles (IDPs), cometary samples (including that from Stardust mission) and, in the insoluble organic matter (IOM) from meteorites [10-12].

Photochemically processed nitrogen within the solar nebula might be one of the sources of enriched ^{15}N (compared to the initial solar value) component. We recently reported a large nitrogen isotopic fractionation in the vacuum ultraviolet (VUV) photodissociation of N_2 performed at temperatures between ambient (300K) and dry ice (~200K)[13]. Here we present new data on the N-isotopic composition in ammonia (measured as N_2) formed by VUV photodissociation of N_2 at

80K temperature using the VUV photons from Advanced Light Source (ALS) synchrotron at the Lawrence Berkeley National Laboratory (LBNL). The lower temperatures are more relevant for astrophysical environments. The new data will be discussed in light of the basic chemical physics and photodissociation dynamics.

II. EXPERIMENTAL TECHNIQUE

VUV photolysis of N_2 was carried out in a differentially pumped reaction chamber, newly designed and built at the ALS to perform the photolysis experiments at different temperatures ranging from 300K (ambient temperature) to 80K by adjusting liquid nitrogen (LN_2) level cooling and subsequent heating of a thermos like reaction chamber shown in Figure 1. A steady flow of high purity premixed gas (N_2: H_2 = 50 : 50) was established in the reaction chamber (kept at 80K) at N_2-partial pressure of 100 mtorr. Photolysis of this gas mixture was carried out at eleven different synchrotron bands (FWHM= 2 nm) between 83 to 98 nm. Photolytically produced atomic N was reacted with hydrogen and the product NH_3 (and NH_2) was initially trapped at the low temperature surface of the reaction chamber. After reaction (~ 8 hours) the chamber was heated to ambient temperature and collected in a sample tube with LN_2. NH_3 yield varied from ~ 0.04 to 6.6 micromoles based on wavelength of photodissociation, photon flux variation during the experiments, and trapping efficiency of the product.

To determine the isotopic composition of product N (trapped in NH_3), NH_3 was decomposed by heating at 800° C in the presence of CuO (prebaked at 900° C) under vacuum[14] and the released N_2 was cryogenically isolated from product water and the dried N_2 was measured for the N-isotopic compositions using a Finnigan MAT 253 IRMS[13].

III. RESULTS

The wavelength dependent N-isotopic fractionation measured at 80K temperatures are shown in Figure 2 along with the previously published results[13]. The summarized data is shown in Table 1. The wavelength dependent fractionation profile is significantly different from that measured at 200K and 300K[13], in each of these relatively higher temperature profiles, there only one ^{15}N enrichment peak was measured at 90 nm (111,111 cm^{-1}, 13.78 eV). However, the low temperature (80K) profile shows multiple peaks (Figure 2). The ^{15}N enrichment at 90 nm is about 9000 ‰ compared to about 12,000 ‰ measured for 200K profile. Moreover, the enrichment profile is extremely sensitive to the wavelength of photodissociation. At some wavelength region (e.g., 88 through 91 nm), the sensitivity is so high that the enrichment values swing between 1000 ‰ and 9000 ‰ several times within this short wavelength span (e.g., 3 nm).

Table 1. N-isotopic compositions measured in the N_2 photodissociation product. All experiments are conducted at 100 mTorr partial pressure of N_2 at a temperature of 80K.

Expt. #	Wavelength (nm)	Energy (eV)	Exposure (min)	N_2 Yield (μmole)	$\delta^{15}N$ (‰)	Blank Corrected $\delta^{15}N$ (‰)	Est. Uncertainty (‰)
ALS-15-02N	83.7	14.82	490	6.64	4492	4500	318
ALS-14-05N	86.7	14.31	480	0.05	1903	2374	192
ALS-14-08N	87.8	14.13	400	0.15	5667	6070	454
ALS-14-03N	88.8	13.97	480	0.43	7931	8120	581
ALS-14-09N	89.1	13.92	360	0.12	4860	5300	393
ALS-14-01N	89.5	13.86	355	0.22	1558	1630	118
ALS-14-04N	90.0	13.78	343	2.47	9009	9046	641
*ALS-15-03N (Repeat)**	*90.0*	*13.78*	*500*	*Alq-1: 0.34*	*8655*	*8917*	*640*
				Alq-II: 1.37	*8826*	*8891*	*631*
ALS-14-02N	91.0	13.62	480	0.16	1020	1088	80
ALS-14-07N	92.5	13.40	420	0.04	2569	3419	291
ALS-14-06N	94.0	13.19	500	1.61	6453	6493	461
ALS-15-01N	97.3	12.74	500	0.51	4033	4803	294

** The NH_3 product (1.71 μmole) from the repeat experiment at 90 nm was divided into two aliquots (0.34 and 1.37 μmole, respectively) and are treated as two different samples. This exercise served two purposes- (i) determine the reproducibility in photodissociation and, (ii) reproducibility in chemical processing of the photochemical products to determine the N-isotopic compositions.*

IV DISCUSSION

(I) VUV photochemistry of N_2

Photoabsorption and photodissociation of N_2 starts in the vacuum ultraviolet (VUV) spectral region, at wavelengths shorter than 100 nm through electric dipole-allowed transitions accessing two valence states (b'$^1\Sigma_u^+$ and b $^1\Pi_u$) and several Rydberg states with $^1\Sigma^+_u$ and $^1\Pi_u$ symmetry from the ground state. The specific electronic states accessible are c´ and b´ $^1\Sigma^+_u$, and c, o, b $^1\Pi_u$ states. Among them c, c´, and o are of Rydberg and b´ and b of valence character. Figure 3 shows the crowded electronic state diagram (diabatic representation) of N_2 depicting significant electrostatic interaction among the different symmetry states apart from the intrinsic configurational mixing within a symmetry group [15-19]. N_2 absorbs photons through slightly broadened partly overlapping rovibrational lines of excited singlet states. Most of the rovibrational levels of the singlet excited states are predissociative. As a consequence, after absorption of photons, the molecule remains bound for nano-second (or less) time scales and, thereafter, dissociates via direct or indirect coupling to a dissociative continuum[20-23]. For indirect coupling cases, the intermediate state is another bound state and couple to the repulsive surface leading to accidental predissociation. Specifically, predissociation occurs through spin-orbit coupling of $^1\Pi_u$ states with a number of states with $^3\Pi_u$ symmetry, including an unbound level, and one state of $^3\Sigma^+_u$ symmetry[18]. Electronic state coupling and, in turn, mixing of rovibrational states is the physical means through which the excited molecule proceeds towards the exit channel and photodissociates into its atomic components. The transition probability of the molecule from one surface to the other in the exit route depends on the overlapping wave functions of the coupled rovibrational states where a greater overlap produces a larger transition probability. Since a probability factor is involved in the process, every molecule that absorbs a photon will not dissociate which leads to <1 quantum

yield for the predissociation process. The molecules which do finally dissociate do so at a different time scale. The molecules with a shorter lifetime (τ) have greater predissociation width and higher predissociation probability (η_{pre})[24, 25]. Therefore, photoabsorption cross-section (σ_{abs}) and photodissociation cross-sections (σ_{dis}) are related by $\sigma_{dis} = \eta_{pre} \times \sigma_{abs}$. For a limited spectral zone (i.e., 95.8 to 96.0 nm, $c'(v'=0)$ level), η_{pre} is shown to be small and thus the dissociation cross-section is drastically different from the absorption cross-section[16]. Another band, $b^1\Pi_u$ ($v=1$), has been studied intensively by different groups [18, 26, 27], is of particular interest because it is the only b-state level which decays principally via radiation, rather than solely by predissociation. As a result, $b(v = 1)$ leads to prominent features in the fluorescence spectrum of N_2, induced both by VUV radiation and electron impact[27]. The measured lifetime of this state is 3.61 ns with predissociation yield of 28%. Most of these studies focused only on the major isotopologue of N_2, e.g., $^{14}N^{14}N$ and without the similar treatment for the minor isotopologue $^{14}N^{15}N$, since the isotopic fractionation in the photodissociation process cannot be determined. It is only recently that a similar calculation for the above mentioned band for minor isotopologues have been performed[18]. The comparison shows that the predissociation probability (η_{pre}) strongly depends on rotational states as well as differing significantly for different isotopologues (Figure 2 of Heays et al.[18]). The spectra for the heavier mass isotopologue shifts towards longer wavelength, with that shift the coupling between different exited states changing significantly and giving rise to varied η_{pre} values for different isotopologues. As the coupling changes with rotational states (different J values), the values of η_{pre} changes with J-values and based on the strength and the nature of the coupling, η_{pre} values for different isotopologues differs. Unfortunately, the same calculation is not available for the entire N_2 photodissociation region, i.e., above first ionization threshold of 79.6 nm to about 100 nm, and η_{pre} was considered to be unity in recent literature[16, 18]. This is a significant assumption

when isotopic fractionation due to photodissociation is calculated. The needed calculations for the entire VUV region are extensive and expensive, therefore, one of the goals of the present research is to shed light on that grey area through precise isotope ratio measurements of the photodissociation product. Moreover, even if the calculation for the entire VUV region for both the isotopologues would have been available, the large uncertainity of these calculated data for determining isotopic fractionation would be of limited value as described below.

(II) Advantage of the present experimental approach

These calculations are based on measurements of cross-sectional (absorption and dissociation) data and the uncertainties in the individual cross-section measurement is about 10% and when the errors are propagated, the effective error could be as high as 20%. The present experiments are at high precision (in ‰) using a gas source mass spectrometer and the ultimate uncertainty is about 5 to 7%, which offers a significant advantage in using these data for cosmochemistry and planetary science applications.

(III) N_2 absorption bands and ALS beam profile

Within the VUV photo absorption zone (i.e., 80- 100 nm), the discrete absorption lines are narrowly spaced. For high precision isotopic ratio measurements, the requirement is of a sufficient amount of analyte (product) gas. Other than the absorption/ dissociation cross-section (σ_a/σ_d), the amount of photodissociation product depends on concentration of the gas in the chamber and the incident photon flux. These two parameters are maximized as far as possible in these experiments. To achieve the maximum possible photon flux, a wide beam was used (by maximizing the Horizontal and Vertical Beam-Defining Apertures (e.g., HBDA and VBDA, respectively [28]) at the synchrotron, which made the synchrotron beam 0.25 eV wide (full width at half maxima, FWHM). Within this wide synchrotron beam, there are several N_2 absorption bands present which will be

excited at the same time (see Table 2 in Appendix). Due to this limitation, the present result is incapable of determining band-by-band ^{15}N fractionations but rather provides an integrated scenario. In any practical applications (e.g., fractionation in planetary atmospheres), the integrated fractionation factors are required for any model and, therefore, the disadvantage of not knowing band-by-band fractionation is redundant.

(IV) Evaluation of isotopic self-shielding in N_2

The line absorption by N_2 is subject to isotopologue self and mutual shielding primarily by absorption of the more abundant $^{14}N_2$ isotopologue resulting in an enrichment of ^{15}N in the dissociation product due to preferential absorption of rarer $^{14}N^{15}N$ and $^{15}N^{15}N$ isotopologues [29, 30]. ^{15}N enrichment profiles over the wavelength range have been computed using a MATLAB program described by Chakraborty et al. [13] based on the concept of isotopologue specific photon absorption (e.g., self-shielding using Beer-Lambert Law). In these computations, the available cross-section data sets from different research groups [3, 16, 18, 21, 31] are inserted separately for the 100, 200 and 300 K temperatures as shown in Figure 4. While computing the enrichment profiles, the same wavelength domains are incorporated as utilized in the experiments. Among the computation, the profiles using the data from [21, 31] show enrichments which are much larger compared to the measured values. For the other profiles, the maximum value of enrichments is comparable to the measured profiles. However, the structure of the wavelength dependent profiles do not match with the measured profile at any temperature. The measured profiles for the temperature of 200K and above show a sharp peak enrichment of ^{15}N at 90 nm, but the computed profiles do not depict any sharp enrichment peak (the peak height of enrichments do vary with wavelengths in the computed profiles). The measured profile at 80K differs from those measured at higher temperatures and show multiple enrichment peaks (88.75, 90 and 94 nm) and display

sharp contrast with the computed profiles generated from cross-sections tabulated in Ref (3, 14, and 16)[3, 16, 18]. These disagreements among the measured and computed profiles suggest that the isotopic self-shielding process might be partially effective for high ^{15}N enrichments, but are greatly modified by the interstate (ro-vibrational) coupling introducing severe perturbations. Given the complexity of the excited electronic state populations, the computed cross-sections using coupled-channel Schrödinger-equation (CSE) treatment[16, 18] may not capture the isotopologue specific fine structure in cross-sectional domain. A related study has shown that while ozone (with a mixture of different isotopologues) was irradiated with narrow linewidth laser, the isotopologue corresponding to that wavelength dissociated proportional to the laser linewidth[32]. The important point this conveys is that irradiating a gas with narrow linewidth is different from that irradiating with a broad beam. The former specifically excites the corresponding isotopologue, whereas the later excites all the isotopologues in its wavelength range and hence the complicated overlapping of the wavefunctions of the excited ro-vibrational states occur, giving rise to large scale perturbations. The present experiments do not measure the isotopic fractionation with high spectral resolution (in energy domain) as a broad beam was used. Provided the experiments were performed with a narrow beam, the effect of isotopic self-shielding would have been dominant as perturbations were minimum. However, for any natural system (as that the solar nebula), the gas medium was exposed to a wider UV/VUV field and hence, the present experiments are most appropriate and as the isotopic ratios are measured in high precision over a wavelength region (Table 1 and Table 2 in appendix), which provides the integrated isotopic fractionation over that wavelength region and are dominated by large scale perturbation subsiding the effect of self-shielding. In the computed profiles, the same wavelength region was incorporated, the mismatch

between the experiment and model is a unique approach to identify the limitations of using only the cross-sectional data to predict isotopic selections in photolysis.

(V) Temperature dependent profile

The significant aspect of this present study is to identify the temperature dependence of the ^{15}N enrichment profile in N_2 photodissociation products. The enrichment profiles at 80K and 200 K are significantly different (Figure 2). These measured profiles are also different from those computed profiles, which are quite monotonous (almost parallel to each other, Figure 4).

As discussed, extensive excited electronic state coupling and mixing resulting in significant perturbations of the electronic states of both symmetries appear to be a common phenomenon during VUV excitation of N_2 molecules. The result of these perturbations are manifested in a wide range of lifetimes for predissociation and are a strong function of isotope masses and is highly sensitive to the excitation wavelength. It was suggested that the strongest isotope effect will occur in spectral regions where states of significantly different oscillator strengths are strongly mixed[33].

Rotational states play a significant role in the predissociation process[25]. Rotational state dependent predissociation yields for $b^1\Pi_u$ ($v=1$) of $^{14}N_2$ have been detected[27]. Heays et al.[18] recently computed the isotopologue ($^{14}N_2$ and $^{14}N^{15}N$) dependent predissociation fraction (η_{pre}) for the same state ($b^1\Pi_u$ ($v=1$)) as a function of rotation level (J), which shows a strong J-dependency of the predissociation process. The computed branching ratio to the decay channels of another excited state of N_2 (e.g., c' ($v'=0$)) also show a strong rotational state dependency[16]. These studies indicate the importance of rotational states in the predissociative photodissociation process. It is also known that the fractional population of a state depends on the temperature, with higher temperatures populating more rotational states[16]. When these two processes are combined, e.g., the temperature dependent population density of J-states and the J-dependent predissociation

process, it is expected that the N_2 photodisociation products should have a temperature dependency.

As discussed, the predissociation process proceeds through transition states from bound electronic to repulsive surfaces and the overlapping wave functions of the interacting states facilitate these transitions with stronger overlaps producing higher transition probabilities. For high temperature configuration, the higher number of *J*-states are populated and possess line broadening (Doppler broadening, Table 2 of Appendix). When *J*-states of all the isotopologues are considered together (isotopologues have same electronic state), due to line broadening, the overlapping wave functions are relatively wider. For lower temperatures, a fewer numbers of *J*-states are occupied and are narrower (less broadening, Table 2) and the resulting overlapping wave functions are also narrower and sparse. The sharper overlapping wave functions should implicate relatively more isotopologue selectivity in the dissociation process compared to the higher temperature scenario. This qualitatively explains the difference in the measured ^{15}N enrichment profiles at high and low temperatures, where at low temperature, the enrichment profile is more structured.

IV. CONCLUSIONS

VUV photodissociation of N_2 at low temperature (80K) show very distinctly different ^{15}N enrichment profile compared to that previously measured at relatively higher temperatures (200 and 300K). At higher temperatures, only one enrichment peak was observed at 90 nm (enrichment peak was much larger at 200K compared to that of 300K). The present enrichment profile shows multiple peaks in the same wavelength regime (80 to 100 nm) including one at 90 nm. A detailed model is required to quantitatively understand the temperature dependence ^{15}N enrichment profiles measured and reported here, which is out of the scope of the present study and these must

incorporate the experimental observations of the temperature and wavelength depenedencies. Rotational states play a major role in predissociation process and the occupational distribution of rotational states is temperature dependent. For predissociation to occur, inter-electronic state crossing is necessary and that only happens when the wave functions of the two ro-vibrational states overlap. This leads the overlapping wave function to become temperature sensitive. We postulate that the measured temperature dependent structure in the ^{15}N enrichment profiles is the manifestation of this inter-electronic state crossing. This new data would be useful in interpreting the nitrogen isotopic fractionations observed in meteoritic materials (signature of solar nebular chemistry), comets, and other planetary atmospheres.

Acknowledgement: The work is funded through NASA's Origins, Cosmochemistry and Emerging Worlds programs. MA, BR, and the ALS are supported by the Director, Office of Energy Res., DOE (Contract No. DE-AC02-05CH11231). SC acknowledge the help from undergraduate student Haiyang Kehoe in experimental work and manuscript preparation.

Appendix

Table 2. Table showing the N_2 absorption bands within each synchrotron bands used in these experiments. Data are taken from the literature [17, 19, 23, 34-39]. For some synchrotron bands, all the incorporated absorption bands are not available and thus no entry in the table for those cases. Line numbers are marked as per the literature mentioned above.

Expt No	Temp (K)	Wave Length (nm)	Wave number (cm^{-1})	$\delta^{15}N$ (‰)	Included Lines	Included States	Wavelength (λ) Range (nm)	λ-Range Value (cm^{-1})	Natural Line Width Γ(cm^{-1})	Doppler Broadening (cm^{-1})	Pressure Broadening (cm^{-1})
ALS-15-02N	84	83.65	119546	4500						0.178	6.52E-06
ALS-14-05N	84	86.67	115300	2374		b'(17)			0.16	0.172	6.52E-06
						o3(5)			0.42		
						c4'(5)			0.51		
						c3(5)			0.27		
						b'(15)			0.16		
ALS-14-06N	84	87.75	114000	6453		o3(5)			0.42	0.170	6.52E-06
						c4'(5)			0.51		
						c3(5)			0.27		
						b'(15)			0.16		
						b'(14)			0.2		
ALS-14-03N	84	88.75	112700	8120		b'(14)			0.2	0.168	6.52E-06
ALS-14-06N	84	89.1	112200	6493						0.167	6.52E-06
ALS-14-01N	84	89.47	111774	1630						0.166	6.52E-06
ALS-14-04N	84	90	111111	9046						0.165	6.52E-06
ALS-15-03N	84	88.75	112700	8120						0.165	6.52E-06
ALS-14-02N	84	91	109900	1089	1	o(2), 1Πu	91.17–91.51	400		0.164	6.52E-06
					2	b(11), 1Πu	91.51–91.74	300			
					3	b'(7), 1Σu	91.74–91.90	200			
ALS-14-07N	84	92.5	108100	3419	2	b(11), 1Πu	91.51–91.74	300		0.161	6.52E-06

						b'(7), 1Σu	91.74–91.90	200			
						c(2), 1Πu	91.90–92.08	200			
						c'(2), 1Σu	92.08–92.24	200			
						b(10), 1Πu	92.24–92.47	300			
						b'(6), 1Σu	92.47–92.77	300			
						o(1) + b(9), 1Πu	92.77–93.08	400			
						b'(5), 1Σu	93.08–93.39	300			
ALS-14-06N	84	94	106380	6493	9	b'(5), 1Σu	93.08–93.39	300		0.158	6.52E-06
					10	b(8), 1Πu	93.39–93.66	300			
					11	b'(4), 1Σu	93.66–93.85	200			
					12	c(1), 1Πu	93.85–93.96	200			
					13	c'(1), 1Σu	93.96–94.15	200			
					14	b(7), 1Πu	94.15–94.41	300			
					15	b'(3), 1Σu	94.41–94.57	200			
					16	o(0), 1Πu	94.57–94.79	200			
ALS-15-01N	84	97.32	102760	4803	23	b(3), 1Πu	96.94–97.62			0.153	6.52E-06
					24	b(2), 1Πu	97.62–98.31				
ALS-13-04N	183	88.99	112360	3341		b'(14)			0.19	0.247	4.42E-06
ALS-13-05N	183	90	111111	3566						0.244	4.42E-06
ALS-13-06N	183	91	109890	3028	1	o(2), 1Πu	91.17–91.51			0.241	4.42E-06
					2	b(11), 1Πu	91.51–91.74				
					3	b'(7), 1Σu	91.74–91.90				
ALS-12-05N	196	80.7	123920	2904						0.282	4.26E-06
ALS-12-06N	196	85.1	117510	2451						0.267	4.26E-06
ALS-11-03N	196	86.67	115380	2690		b'(17))			0.15	0.262	4.26E-06
						o3(5)			0.42		
						c4'(5)			0.46		
						c3(5)			0.27		
						b'(15			0.15		

ALS-11-05N	196	88.56	112920	3112		b'(15)		0.15	0.257	4.26E-06
						b'(14)		0.19		
ALS-12-02N	196	90	111111	11750					0.253	4.26E-06
ALS-12-03N	196	92	108700	2887	1 2 3 4 5 6 7	o(2), 1Πu	91.17–91.51		0.247	4.26E-06
						b(11), 1Πu	91.51–91.74			
						b'(7), 1Σu	91.74–91.90			
						c(2), 1Πu	91.90–92.08			
						c'(2), 1Σu	92.08–92.24			
						b(10), 1Πu	92.24–92.47			
						b'(6), 1Σu	92.47–92.77			
ALS-12-04N	196	94	106380	2904	9	b'(5), 1Σu	93.08–93.39		0.242	4.26E-06
					10	b(8), 1Πu	93.39–93.66			
					11	b'(4), 1Σu	93.66–93.85			
					12	c(1), 1Πu	93.85–93.96			
					13	c'(1), 1Σu	93.96–94.15			
					14	b(7), 1Πu	94.15–94.41			
					15	b'(3), 1Σu	94.41–94.57			
					16	o(0), 1Πu	94.57–94.79			
ALS-11-06N	196	96.11	104050	1229	19	b(5), 1Πu	95.31–95.68		0.237	4.26E-06
					20	c'(0) + b'(1), 1Σu	95.68–95.95			
					21	c(0), 1Πu	95.95–96.29			
					22	b(4) + b'(0), 1Πu/1Σu	96.29–96.94			
ALS-12-01N	196	97	103090	937	22	b(3), 1Πu	96.29–96.94		0.234	4.26E-06
					23	b(2), 1Πu	96.94–97.62			

ALS-11-04N	196	97.9	102150	967	23	b(3), 1Πu	96.94–97.62		0.232	4.26E-06
					24	b(2), 1Πu	97.62–98.31			
					25	b(1), 1Πu	98.31–98.89			
ALS-13-09N	224	93.9	105600	1734	9	b'(5), 1Σu	93.08–93.39		0.259	3.99E-06
					10	b(8), 1Πu	93.39–93.66			
					11	b'(4), 1Σu	93.66–93.85			
					12	c(1), 1Πu	93.85–93.96			
					13	c'(1), 1Σu	93.96–94.15			
					14	b(7), 1Πu	94.15–94.41			
					15	b'(3), 1Σu	94.41–94.57			
					16	o(0), 1Πu	94.57–94.79			
ALS-13-10N	234	91.5	109290		1	o(2), 1Πu	91.17–91.51		0.272	3.91E-06
					2	b(11), 1Πu	91.51–91.74			
					3	b'(7), 1Σu	91.74–91.90			
					4	c(2), 1Πu	91.90–92.08			
					5	c'(2), 1Σu	92.08–92.24			
					6	b(10), 1Πu	92.24–92.47			
ALS-13-12N	264	90	111111	9874					0.293	3.68E-06
ALS-13-11N	269	90	111111	10457					0.296	3.64E-06
ALS-13-07N	297	86.67		3020		b'(17)		0.14	0.323	3.47E-06
						o3(5)		0.42		
						c4'(5)		0.46		
						c3(5)		0.27		
						b'(15)		0.14		
ALS-13-01N	297	88.56	112920	1796		b'(15)		0.14	0.316	3.47E-06
						b'(14)		0.19		
ALS-13-02N	297	90	111111	2965					0.311	3.47E-06
ALS-13-03N	297	91.5	109290	2332	1	o(2), 1Πu	91.17–91.51		0.306	3.47E-06
					2	b(11), 1Πu	91.51–91.74			
					3	b'(7), 1Σu	91.74–91.90			

					4	c(2), 1Πu	91.90–92.08		
					5	c'(2), 1Σu	92.08–92.24		
					6	b(10), 1Πu	92.24–92.47		
ALS-11-01N	297	93.93	106470	1506	9	b'(5), 1Σu	93.08–93.39	0.298	3.47E-06
					10	b(8), 1Πu	93.39–93.66		
					11	b'(4), 1Σu	93.66–93.85		
					12	c(1), 1Πu	93.85–93.96		
					13	c'(1), 1Σu	93.96–94.15		
					14	b(7), 1Πu	94.15–94.41		
					15	b'(3), 1Σu	94.41–94.57		
					16	o(0), 1Πu	94.57–94.79		
ALS-13-08N	297	96.22	103932	1734	19	b(5), 1Πu	95.31–95.68	0.291	3.47E-06
					20	c'(0) + b'(1), 1Σu	95.68–95.95		
					21	c(0), 1Πu	95.95–96.29		
					22	b(4) + b'(0), 1Πu/1Σu	96.29–96.94		
ALS-11-02N	297	97.32	102760	648	23	b(3), 1Πu	96.94–97.62	0.288	3.47E-06
					24	b(2), 1Πu	97.62–98.31		

References:

1. M. H. Thiemens, S. Chakraborty and G. Dominguez, Annual Review of Physical Chemistry **63** (1), 155-177 (2012).
2. R. R. Meier, J. A. R. Samson, Y. Chung, E. M. Lee and Z. X. He, Planetary and Space Science **39** (8), 1197-1207 (1991).
3. M.-C. Liang, A. N. Heays, B. R. Lewis, S. T. Gibson and Y. L. Yung, The Astrophysical Journal Letters **664** (2), L115 (2007).
4. S. Chakraborty, P. Yanchulova and M. H. Thiemens, Science **342** (6157), 463-466 (2013).
5. B. Marty, M. Chaussidon, R. C. Wiens, A. J. G. Jurewicz and D. S. Burnett, Science **332** (6037), 1533-1536 (2011).
6. E. Furi and B. Marty, Nature Geosci **8** (7), 515-522 (2015).
7. J. F. Kerridge, Geochimica et Cosmochimica Acta **49** (8), 1707-1714 (1985).
8. C.-C. Kung and R. N. Clayton, Earth and Planetary Science Letters **38** (2), 421-435 (1978).
9. M. M. Grady, I. P. Wright, L. P. Carr and C. T. Pillinger, Geochimica et Cosmochimica Acta **50** (12), 2799-2813 (1986).
10. H. Busemann, A. F. Young, C. M. O. D. Alexander, P. Hoppe, S. Mukhopadhyay and L. R. Nittler, Science **312** (5774), 727-730 (2006).
11. K. D. McKeegan, J. Aléon, J. Bradley, D. Brownlee, H. Busemann, A. Butterworth, M. Chaussidon, S. Fallon, C. Floss, J. Gilmour, M. Gounelle, G. Graham, Y. Guan, P. R. Heck, P. Hoppe, I. D. Hutcheon, J. Huth, H. Ishii, M. Ito, S. B. Jacobsen, A. Kearsley, L. A. Leshin, M.-C. Liu, I. Lyon, K. Marhas, B. Marty, G. Matrajt, A. Meibom, S. Messenger, S. Mostefaoui, S. Mukhopadhyay, K. Nakamura-Messenger, L. Nittler, R. Palma, R. O. Pepin, D. A. Papanastassiou, F. Robert, D. Schlutter, C. J. Snead, F. J. Stadermann, R. Stroud, P. Tsou, A. Westphal, E. D. Young, K. Ziegler, L. Zimmermann and E. Zinner, Science **314** (5806), 1724-1728 (2006).

12. G. Briani, M. Gounelle, Y. Marrocchi, S. Mostefaoui, H. Leroux, E. Quirico and A. Meibom, Proceedings of the National Academy of Sciences **106** (26), 10522-10527 (2009).
13. S. Chakraborty, B. H. Muskatel, T. L. Jackson, M. Ahmed, R. D. Levine and M. H. Thiemens, Proceedings of the National Academy of Sciences **111** (41), 14704-14709 (2014).
14. L. Li, P. Cartigny and M. Ader, Geochimica Et Cosmochimica Acta **73** (20), 6282-6297 (2009).
15. H. Lefebvre-Brion and B. R. Lewis, Molecular Physics **105** (11-12), 1625-1630 (2007).
16. X. Li, A. N. Heays, R. Visser, W. Ubachs, B. R. Lewis, S. T. Gibson and E. F. van Dishoeck, A&A **555**, A14 (2013).
17. A. N. Heays, G. D. Dickenson, E. J. Salumbides, N. d. Oliveira, D. Joyeux, L. Nahon, B. R. Lewis and W. Ubachs, The Journal of Chemical Physics **135** (24), 244301 (2011).
18. A. N. Heays, R. Visser, R. Gredel, W. Ubachs, B. R. Lewis, S. T. Gibson and E. F. van Dishoeck, A&A **562**, A61 (2014).
19. B. R. Lewis, A. N. Heays, S. T. Gibson, H. Lefebvre-Brion and R. Lefebvre, Journal of Chemical Physics **129** (16), 10 (2008).
20. D. Stahel, M. Leoni and K. Dressler, The Journal of Chemical Physics **79** (6), 2541-2558 (1983).
21. D. Spelsberg and W. Meyer, The Journal of Chemical Physics **115** (14), 6438-6449 (2001).
22. J. P. Sprengers, W. Ubachs, K. G. H. Baldwin, B. R. Lewis and W. U. L. Tchang-Brillet, Journal of Chemical Physics **119** (6), 3160-3173 (2003).
23. G. Stark, K. P. Huber, K. Yoshino, P. L. Smith and K. Ito, Journal of Chemical Physics **123** (21) (2005).
24. B. R. Lewis, S. T. Gibson, W. Zhang, H. Lefebvre-Brion and J.-M. Robbe, The Journal of Chemical Physics **122** (14), 144302 (2005).
25. B. R. Lewis, S. T. Gibson, J. P. Sprengers, W. Ubachs, A. Johansson and C. G. Wahlstrom, The Journal of Chemical Physics **123** (23), 236101-236103 (2005).
26. J. P. Sprengers, W. Ubachs, A. Johansson, A. L'Huillier, C.-G. Wahlström, R. Lang, B. R. Lewis and S. T. Gibson, The Journal of Chemical Physics **120** (19), 8973-8978 (2004).

27. C. Y. R. Wu, D. L. Judge, M.-H. Tsai, Y.-C. Lin, T.-S. Yih, J.-I. Lo, H.-S. Fung, Y.-Y. Lee, B. R. Lewis, A. N. Heays and S. T. Gibson, The Journal of Chemical Physics **136** (4), 044301 (2012).
28. P. A. Heimann, M. Koike, C. W. Hsu, D. Blank, X. M. Yang, A. G. Suits, Y. T. Lee, M. Evans, C. Y. Ng, C. Flaim and H. A. Padmore, Review of Scientific Instruments **68** (5), 1945-1951 (1997).
29. R. N. Clayton, Nature **415** (6874), 860-861 (2002).
30. M. H. Thiemens and J. E. Heidenreich, Science **219** (4588), 1073-1075 (1983).
31. B. H. Muskatel, F. Remacle and R. D. Levine, The Journal of Physical Chemistry A **116** (46), 11311-11318 (2012).
32. H. Kuze, T. Sato, T. Kambe, S. Hayashida and Y. Tatsumi, Chemical Physics Letters **455** (4–6), 156-158 (2008).
33. B. H. Muskatel, F. Remacle, M. H. Thiemens and R. D. Levine, Proceedings of the National Academy of Sciences **108** (15), 6020 (2011).
34. W. Ubachs, Chemical Physics Letters **268** (1-2), 201-206 (1997).
35. G. Stark, B. R. Lewis, A. N. Heays, K. Yoshino, P. L. Smith and K. Ito, The Journal of Chemical Physics **128** (11), 114302-114310 (2008).
36. G. Stark, B. R. Lewis, A. N. Heays, K. Yoshino, P. L. Smith and K. Ito, The Journal of Chemical Physics **128** (11), 114302 (2008).
37. B. R. Lewis, K. G. H. Baldwin, A. N. Heays, S. T. Gibson, J. P. Sprengers, W. Ubachs and M. Fujitake, Journal of Chemical Physics **129** (20) (2008).
38. J. P. Sprengers, W. Ubachs and K. G. H. Baldwin, The Journal of Chemical Physics **122** (14), 144301-144306 (2005).
39. J. P. Sprengers, E. Reinhold, W. Ubachs, K. G. H. Baldwin and B. R. Lewis, The Journal of Chemical Physics **123** (14), 144315 (2005).
40. A. N. Heays, J. M. Ajello, A. Aguilar, B. R. Lewis and S. T. Gibson, The Astrophysical Journal Supplement Series **211** (2), 28 (2014).

Figure Captions

Figure 1. Schematic diagram of the newly designed and fabricated LN_2 cooled reaction chamber to perform photolysis experiments at various temperatures. The design of the chamber was similar to a thermos with three coaxial cylinders (with increasing diameters) were welded together creating three compartments made out of stainless steel (SS). The innermost compartment was the reaction chamber, the second compartment was the LN_2 reservoir and the third (outermost) compartment was a vacuum chamber (kept under high vacuum using a turbo pump for temperature stabilization by reduce the evaporation rate). The reaction chamber compartment was fabricated with a long SS bellow to increase the surface of the reaction chamber. The chamber was attached through a 2 mm orifice to a three-stage differential pumping system (DPS). The other end of the DPS is connected to the beamline (9.0.2) end station through a gate valve.

Figure 2. ^{15}N enrichment profiles of the photodissociation product of N_2 at three different temperatures: 80K (new data), 200K and 300K[13]. N_2 dissociation product atomic N was captured as NH_3 (and NH_2) by reacting with hydrogen inside the chamber. At the end of the reaction, NH_3 was isolated cryogenically and decomposed to N_2 (see text for details) and measured in the mass spectrometer for isotopic composition. The high temperature (200 and 300K) profiles show a peak in ^{15}N enrichment at 90 nm (111,111 cm^{-1}). The new 80K data shows multiple enrichment peaks (88.75 and 94 nm) apart from the one at 90 nm.

Figure 3. Potential energy diagram of N_2 in diabetic representation adopted from Vieitez et al., 2008, Li et al., 2013 and Heays et al., 2014. The interstate crossings are prominent in the high energy domain, which introduce perturbations to the system.

Figure 4. ^{15}N enrichment profiles over the wavelength range have been computed using a MATLAB program described by Chakraborty et al., 2014[13], based on the concept of isotopologue specific photon absorption (e.g., self-shielding using Beer-Lamert Law). In these computations the available cross-sectional data sets from different research groups (DL=Liang et al., 2007[3]; SM=Spelsberg and Mayer, 2001[21], Muskatel et al., 2012[31]; ANU= Li et al., 2013[16], Heays et al., 2014[40]) are inserted separately for the 100, 200 and 300 K temperatures. The measured profiles for 80 K and 200 K are also plotted along with the computed profiles for comparison.

Figures

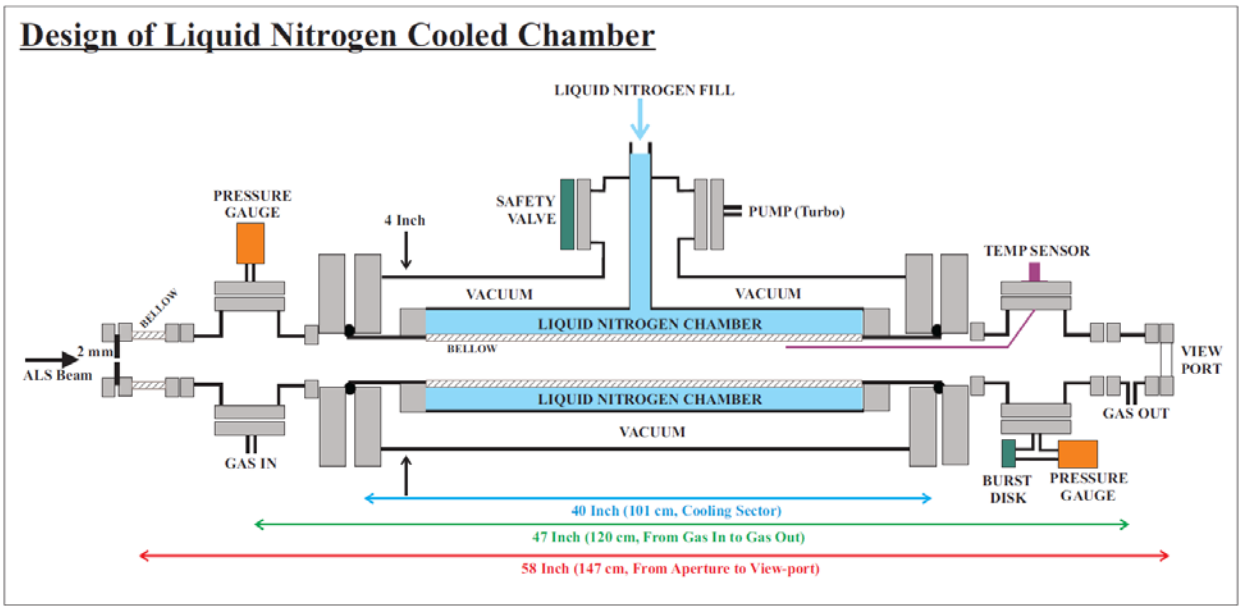

Figure 1

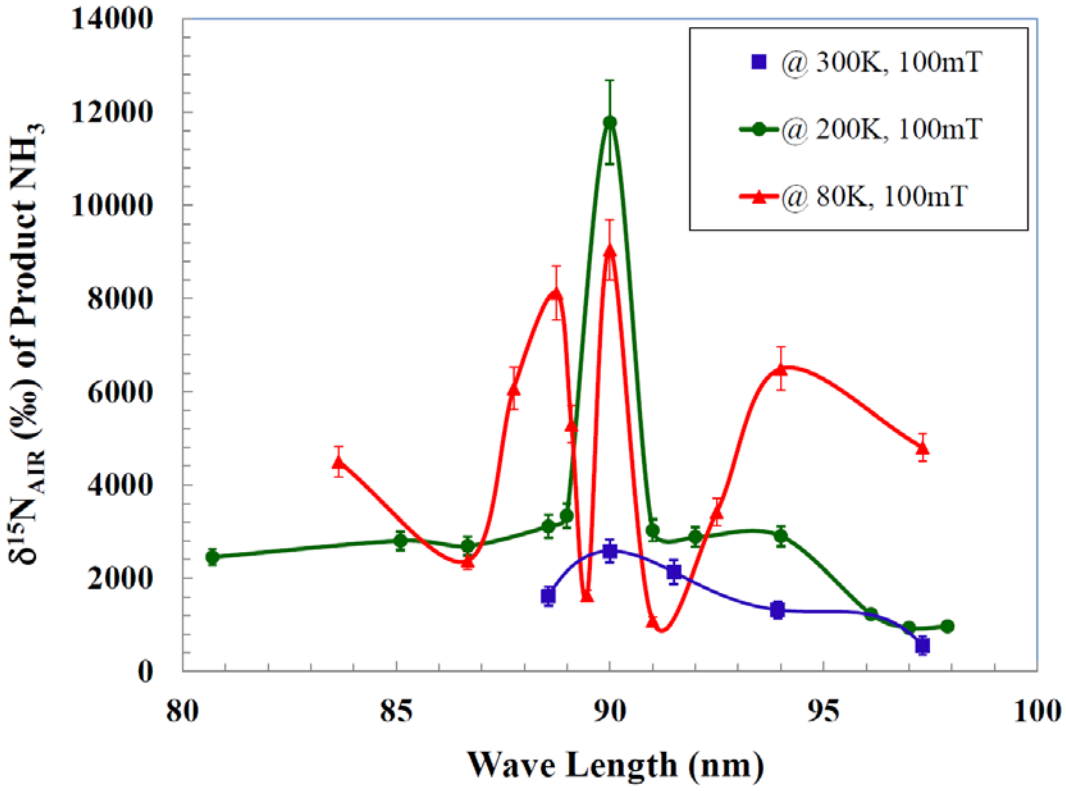
14000
12000
10000
8000
6000
4000
2000
0
80
85
90
95
100
δ15NAIR (‰) of Product NH3
Wave Length (nm)
@ 300K, 100mT
@ 200K, 100mT
@ 80K, 100mT

Figure 2

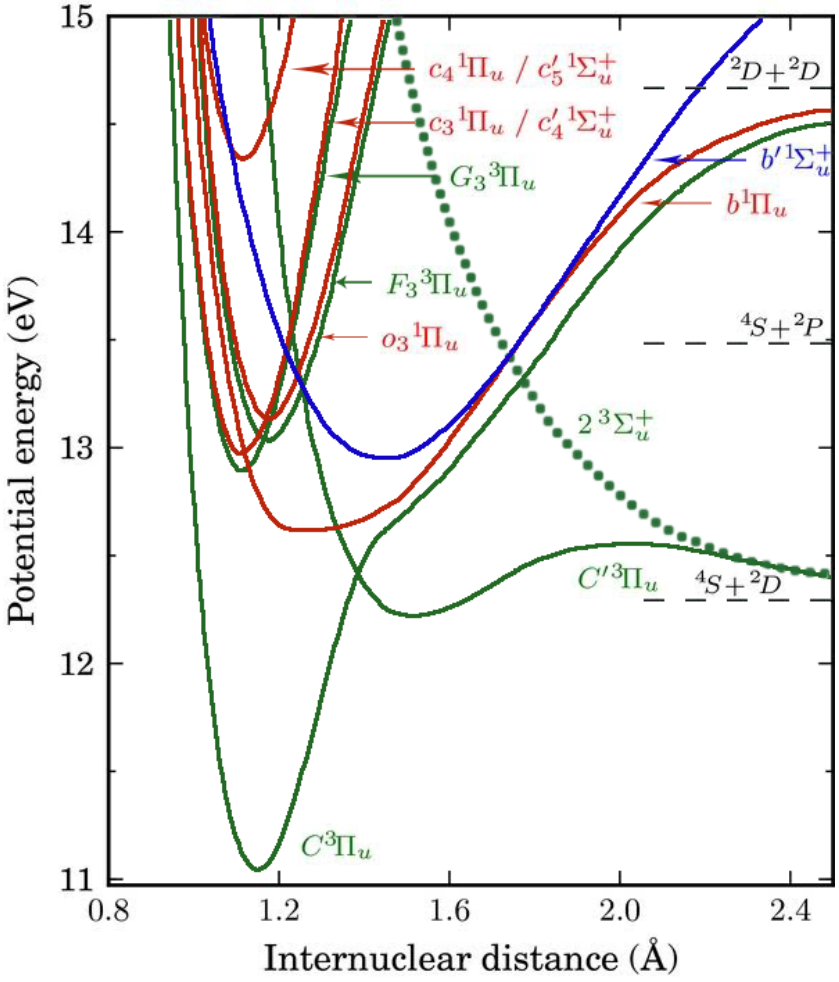
15
14
13
12
11
0.8
1.2
1.6
2.0
2.4
Potential energy (eV)
Internuclear distance (Å)
$c_4\,^1\Pi_u$ / $c_5'\,^1\Sigma_u^+$
$c_3\,^1\Pi_u$ / $c_4'\,^1\Sigma_u^+$
$G_3\,^3\Pi_u$
$F_3\,^3\Pi_u$
$o_3\,^1\Pi_u$
$C\,^3\Pi_u$
$2\,^3\Sigma_u^+$
$C'\,^3\Pi_u$
$b'\,^1\Sigma_u^+$
$b\,^1\Pi_u$
$^2D+^2D$
$^4S+^2P$
$^4S+^2D$

Figure 3

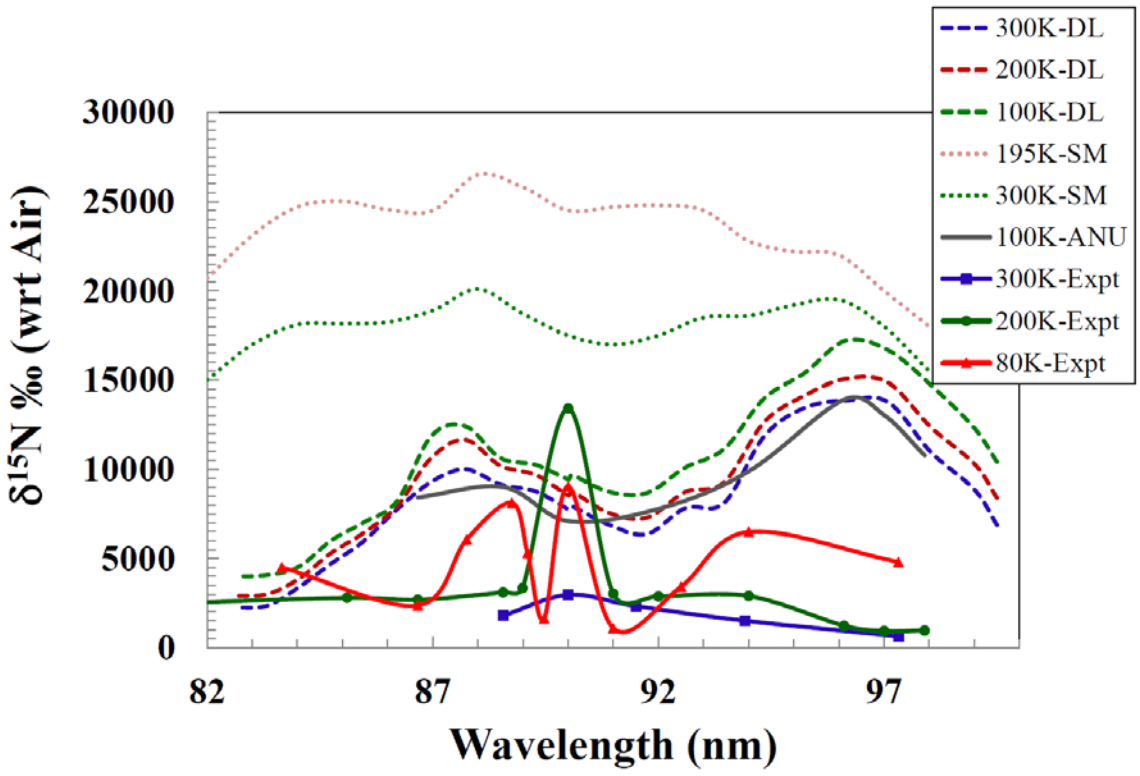
300K-DL
200K-DL
100K-DL
195K-SM
300K-SM
100K-ANU
300K-Expt
200K-Expt
80K-Expt
30000
25000
20000
15000
10000
5000
0
δ15N ‰ (wrt Air)
82
87
92
97
Wavelength (nm)

Figure 4